COPYRIGHT NOTICE

M. Lacerenza, M. Buttafava, M. Renna, A. Dalla Mora, L. Spinelli, F. Zappa, A. Pifferi, A. Torricelli, A. Tosi, D. Contini

Wearable and wireless time-domain near-infrared spectroscopy system for brain and muscle hemodynamic monitoring

MICHELE LACERENZA,[1,4] **MAURO BUTTAFAVA,**[2] **MARCO RENNA,**[2] **ALBERTO DALLA MORA,**[1] **LORENZO SPINELLI,**[3] **FRANCO ZAPPA,**[2] **ANTONIO PIFFERI,**[1,3] **ALESSANDRO TORRICELLI,**[1,3] **ALBERTO TOSI,**[2] **AND DAVIDE CONTINI**[1,5]

[1]*Dipartimento di Fisica, Politecnico di Milano, 20133 Milano, Italy*
[2]*Dipartimento di Elettronica, Informazione e Bioingegneria, Politecnico di Milano, 20133 Milano, Italy*
[3]*Istituto di Fotonica e Nanotecnologie, Consiglio Nazionale delle Ricerche, 20133 Milano, Italy*
[4]*michele.lacerenza@polimi.it*
[5]*davide.contini@polimi.it*

Abstract: We present a wearable time-domain near infrared spectroscopy (TD-NIRS) system (two wavelengths, one detection channel), which fits in a backpack and performs real-time hemodynamic measurements on the brain and muscle tissues of freely moving subjects. It can provide concentration values of oxygenated hemoglobin (O_2Hb), deoxygenated hemoglobin (HHb), total hemoglobin (tHb = O_2Hb + HHb) and tissue oxygen saturation (StO_2). The system is battery-operated and can be wirelessly controlled. By following established characterization protocols for performance assessment of diffuse optics instruments, we achieved results comparable with state-of-the-art research-grade TD-NIRS systems. We also performed *in-vivo* measurements such as finger tapping (motor cortex monitoring), breath holding (prefrontal cortex monitoring and forearm muscle monitoring), and outdoor bike riding (vastus lateralis muscle monitoring), in order to test the system capabilities in evaluating both muscle and brain hemodynamics.

1. Introduction

Near infrared spectroscopy (NIRS) is a non-invasive tool for tissue characterization and monitoring [1]. NIRS can retrieve the concentration of oxy-hemoglobin (O_2Hb), deoxy-hemoglobin (HHb), and consequently the total amount of hemoglobin (tHb = O_2Hb + HHb) and the tissue oxygen saturation ($StO_2 = O_2Hb$/tHb) by estimating the absorption coefficient at two or more wavelengths in the near infrared region (between 600 nm and 1000 nm) [2]. The continuous monitoring of these parameters can give important information about tissue (e.g., brain, muscle) activity and can have a high impact on clinical applications [3].

NIRS has been implemented in three main modalities that differ from each other based on the temporal characteristics of the employed light: continuous-wave NIRS (CW-NIRS: light with constant intensity [4]), frequency-domain NIRS (FD-NIRS: modulated light intensity) and time-domain NIRS (TD-NIRS: pulsed light intensity) [5]. Regardless the type of technique, the possibility to successfully apply NIRS instruments in clinical environment requires the following main features: accuracy, depth sensitivity, and selectivity (the capability to distinguish between the different tissue layers), reliability, robustness, and compactness. TD-NIRS can disentangle scattering from absorption information, improving the accuracy in the hemodynamics assessment [5]. The depth information naturally encoded in the TD-NIRS measurements also improves its depth sensitivity [6] and its rejection capability of measurement artifacts (movement artifacts, instrument drifts, etc.) ensures more reliable results compared to other techniques [7].

The complexity of TD-NIRS devices, mainly related to the need for narrow-pulse laser sources, time-resolved single-photon detectors, and high-precision timing electronics, usually brings to bulkiness, high cost and difficult usage. These issues limited the widespread adoption of TD-NIRS instruments, despite their interesting features [5]. In previous works [8,9] we demonstrated the possibility to improve robustness and reduce the dimension of a dual-wavelength, one detection channel TD-NIRS system employing custom photodetectors and pulsed-diode lasers. In this work, we present the in-depth characterization of such a device and demonstrate its capabilities in muscle and brain measurements. The device is now wearable, battery-operated, and remotely controlled. These features bring tremendous advantages for *in-vivo* measurements, leading to the possibility of brain and muscle monitoring on freely moving subjects with comparable accuracy and reliability to the state-of-the-art TD-NIRS instruments.

2. System description

The instrument architecture is sketched in Fig. 1(a). The system has one detection channel and employs a time-multiplexing measurement scheme [10], to prevent wavelength crosstalk. In fact, the same detector collects photons at different wavelengths, sequentially injected into the sample.
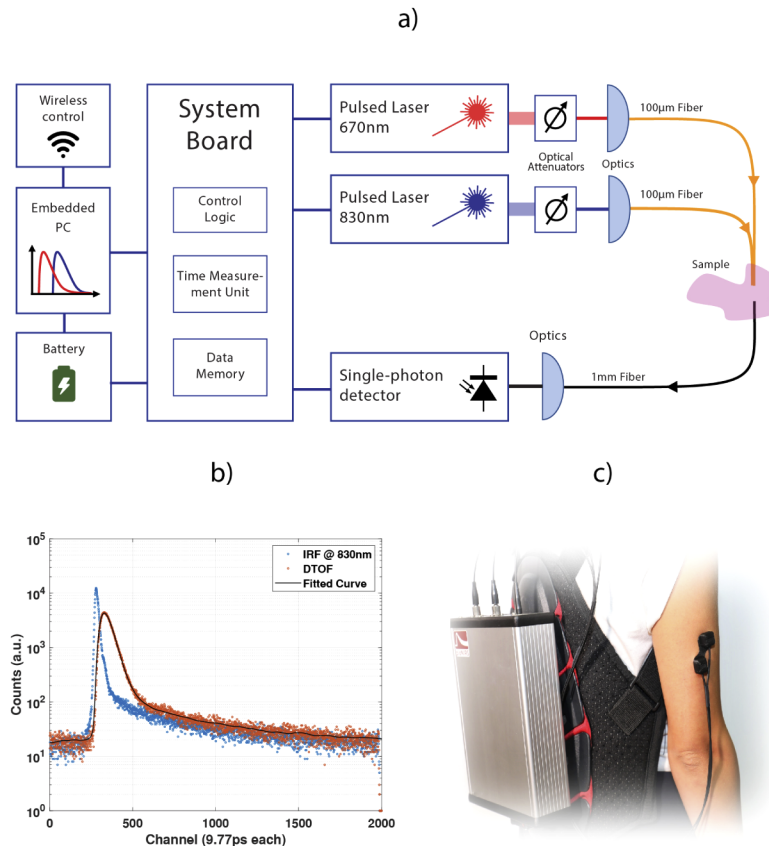
Fig. 1. (a) Simplified block diagram of the instrument. (b) DTOF curve, collected from brain tissue, in red. The IRF of the system is shown in blue. The black curve is the result of the fitting [14] of the experimental DTOF. (c) Custom made backpack holder to wear the system during in-vivo measurements, in the picture the probe is positioned on the right arm as example.

As light source, we included a couple of pulsed-diode lasers, operating in gain-switching mode at 50 MHz repetition rate, emitting light at 670 nm (4 mW, average output power) and 830 nm (3.5 mW, average output power), respectively. The custom-made laser driving electronics [8] is tailored to guarantee stability over time, both in terms of optical power and pulse shape. For each wavelength, laser light passes through a custom-made motorized optical attenuator and then is coupled to a 100 μm graded-index glass optical fiber (NA = 0.29, by F.M.C., Italy). To create a single injection point, fibers from the two laser sources are bundled together. A graded-index plastic optical fiber (POF), with a core diameter of 0.9 mm, collects light backscattered from the tissue (NA = 0.29, by FiberFin, Inc., USA). A 3D-printed flexible probe hosts both injection and detection fibers. Optical fibers are coupled to the tissue by means of a prism, which bends light of 90°, thus making it possible to keep the fibers parallel to the probed surface, for improved contact during movement of the probed tissue. The distance between injection and collection points on the sample surface is 3 cm. Backscattered photons are detected by a silicon photomultiplier (SiPM) [11] with an active area of (1.3×1.3 mm^2) coupled to the detection fiber. Both the coupling optics and the single-photon detector module are custom-made [12]. A time-to-digital converter (TDC) application-specific integrated circuit (ASIC) [13] with 10 ps resolution, measures the arrival-times of detected photons reconstructing the optical waveforms (i.e. distribution of photons time of flight, DTOF). Figure *1*(b) shows a typical DTOF curve, obtained during an *in-vivo* measurement and the instrument response function (IRF) of the system, both at 830 nm wavelength. The system is operated via a 14.8 V Li-ion battery (Ansmann AG, Germany) and exhibits an average power consumption of around 10 W, translating into more than 6 hours of battery lifetime, without any degradation in measurement performance. The instrument is controlled by an embedded PC (DFRobot 4G/64G), with Windows 10 OS, allowing for wireless remote operation via Wi-Fi or Bluetooth. The system is lightweight enough (2.5 kg) to be easily worn as a backpack, as shown. A custom software easily controls the hardware and the measurements, making it possible to acquire and analyze data in real-time with a measurement rate up to 2 Hz.

3.　Data analysis

In this study, different procedures have been followed to analyze the collected data. On phantom measurements, for the *in-vivo* monitoring of muscle and the baseline measurements on the brain (i.e., the acquisition of baseline physiological parameters), the probed samples were considered as homogeneous media. Then, each DTOF curve was fitted by an analytical model for photon diffusion in a semi-infinite homogeneous medium after convolution with the IRF [14], to retrieve absorption (μ_a) and reduced scattering (μ_s') coefficients. For functional measurements on brain cortex, instead, the sample was considered a two-layer medium (extracerebral layer, with an equivalent thickness of 0.5 cm, followed by the cerebral cortex) and an empirical model based on the estimate of the photon mean time-dependent pathlength (MTP) was used [15]. According to this method, starting from 80% of the rising edge, each DTOF was divided in 10 consecutive time-gates with 400 ps width and the extra-cerebral and intra-cerebral MTPs were estimated for each gate. The changes in the absorption coefficients concerning the baseline in the extra-cerebral and intra-cerebral layers were then derived for all wavelengths. Hemodynamic parameters (absolute concentration of oxygenated hemoglobin, O_2Hb and deoxygenated hemoglobin, HHb) were calculated from the absolute absorption coefficients (baseline value plus change) employing the Beer's law.

4.　Phantom experiments

We carried out an in-depth characterization of the device, by following three well-established protocols to assess the performances of diffuse optics devices, namely: MEDPHOT [16], BIP [17] and nEUROPt [18]. Specifically, the measurement stability was assessed following the

BIP protocol, whereas the nEUROPt protocol was exploited to assess depth sensitivity. Further, linearity, noise, and reproducibility were assessed on phantom adopting the MEDPHOT protocol guidelines. In addition to the standard characterization, we performed extra measurements to assess the instrument performance related to *in-vivo* settings for what concerns the reproducibility and the long-term repeatability of the acquisitions. A detailed description of all the tests is reported in the followings.

4.1. Stability

The system has been tested on a 15 hours stability measurement, to assess its performance over a long period of time, under the same experimental conditions. The probe was placed on an IRF box, which is a black box with a mirror surface on the bottom to permit easy acquisition of the IRF in reflectance geometry without disassembling the probe [19]. Integration time was set to 1 s per wavelength and the photodetector count rate to about 10^6 counts per second. The stability measurement started 3 minutes after turning on the instrument, therefore the first three minutes of warmup time happened during the setting up of the experiment and are not shown here.

In Fig. 2(a), the values of count rate (photons/s), IRF barycenter (ps), and IRF full width at half maximum (FWHM) (ps) during the stability measurement for the 830 nm laser source are reported. Results at 670 nm showed comparable behavior. Plots of Fig. 2(b) show the first 216 s of each measurement, in order to highlight the performance of the system during the warmup time. The total warm up time lasted approximately 5 minutes. The black dashed lines show the boundaries within which values can be considered stable (for typical NIRS measurements) after the first minutes of warm-up. The integrated counts per second fall within ±1% from the mean value over all 15 h. The barycenter of the IRF stays within ±2 ps from its mean, and the FWHM shows less than 5% oscillations over the 15 h period. Those values are commonly considered as optimal boundaries for TD-NIRS instrumentation's stability features [8,10,17].
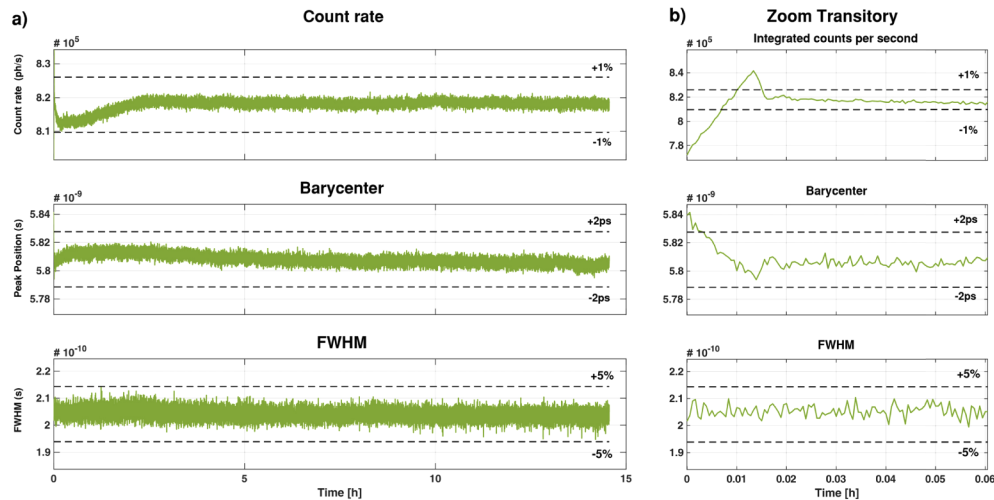
Fig. 2. (a) 15 h stability measurements of the system, using an IRF box in reflectance mode. The time behavior of count rate, barycenter and FWHM are reported in different rows. All data refer to 830 nm wavelength. Acceptable values during the stability fall within the dashed lines with respect to the mean value of the measurements. (b) A zoom of the first 216 s of the stability measurements is reported to better appreciate the warm-up transition.

4.2. Depth sensitivity

The nEUROPt protocol was specifically developed to measure the capability of instruments for optical brain imaging to detect, localize, and quantify changes in the optical properties of the brain. It is focused on the evaluation of sensitivity and spatial resolution in non-homogeneous turbid media. Here we present the results for the depth sensitivity of the system. We adopted the equivalent black volume (EBV) concept, stating that a single totally absorbing inclusion of a given volume provides the same optical perturbation of a variety of realistic absorption inhomogeneities with different combinations of shape, volume and absorption properties [20]. Measurements were performed placing the probe in different positions on a solid, tissue-mimicking phantom ($\mu_a = 0.07\ cm^{-1}$, $\mu_s' = 10\ cm^{-1}$, nominal values at 660 nm), hosting a sliding rod with same optical features plus a totally absorbing inclusion in the middle [18]. Placing the rod between the injection and collection points (3 cm inter-fiber distance), the inclusion (black cylinder with 5 mm diameter x 5 mm height, corresponding to EBV = 98 mm^3) is moved deep into the phantom thanks to a motor that translates the rod at steps of 1 mm for a total depth of 5 cm. Inclusion's depth is referred to the center of the black cylinder. Measurements were taken with 500 ms integration time, 10^6 photons/s and 20 repetitions at each step. For the contrast analysis, the DTOF curves have been divided into two time-windows also called time gates. Sensitivity is evaluated considering the change in detected photon counts for different rod positions when the inclusion is moving away from the probe, by using the relative contrast $C_{g,i}$, defined as:

$$C_{g,i} = \frac{N_{g,0} - N_{g,i}}{N_{g,0}}, \tag{1}$$

where $N_{g,i}$ is the detected number of photons at step i for time-gate g, $N_{g,0}$ is the detected number of photons for the same time-gate g at 35 mm inclusion's depth (corresponding to the homogeneous unperturbed case). In Fig. 3(a), the relative contrast $C_{g,i}$ at 830 nm is shown for two different gates: an early gate from 0 ps (the peak position of the IRF) to 800 ps, and a late gate from 2000 ps to 3200 ps. As expected, the contrast peak position is shifted towards deeper inclusion positions in case of the late gate (13.5 mm *vs.* 10 mm), thanks to the higher sensitivity to deeper perturbations of late gates compared to early ones. To better appreciate how well the system can distinguish the perturbation compared to the homogeneous case, it is worth taking into consideration the contrast-to-noise ratio (CNR) at time gate g and step i:

$$CNR_{g,i} = \frac{N_{g,0} - N_{g,i}}{\sqrt{N_{g,0}}}, \tag{2}$$

where $\sqrt{N_{g,0}}$ represents the standard deviation due to the Poisson noise, considered as the main noise source present in the measurements. From Fig. 3(b), it is possible to see that in the late gate, the system shows a CNR higher than one until a depth of about 30 mm. The y-axis in Fig. 3(b) is limited to CNR=1 as lower boundary. Any result with CNR<1, which is due to noise fluctuations and slight phantom inhomogeneity, are therefore not shown.

4.3. Linearity

To assess the linearity of the instrument in measuring μ_s' and μ_a, a set of 32 solid phantoms with a wide range of optical properties (μ_a ranging from 0 to 0.49 cm^{-1}, and μ_s' from 5 to 20 cm^{-1} [21–23] was used. The nominal values for the optical parameters of the solid phantoms were retrieved from a characterization performed by a state-of-the-art laboratory-grade system [24]. The measurement protocol consisted of 20 repetitions with 1 s integration time per wavelength, the device showed good linearity (both for μ_s' and μ_a) for both wavelengths; results are shown in Fig. 4. In the case of the absorption coefficient, each point on the graph shows the average measured μ_a value for the set of phantoms with the same nominal μ_a and different nominal μ_s'. On
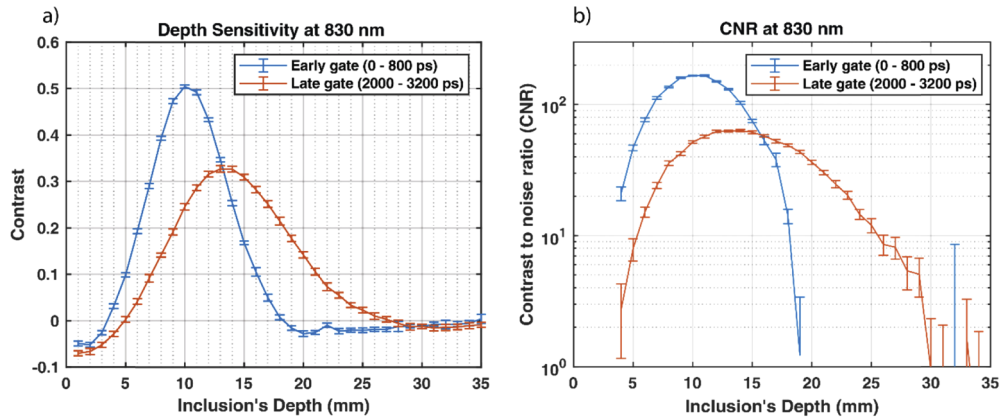
Fig. 3. Measured contrast (a) and contrast-to-noise ratio (b) at different inclusion depths for two different time windows of the DTOF curve. Early gate (blue curve) is taken from 0 to 800 ps, while late gate (red curve) from 2000 to 3200 ps. Error bars are calculated over 20 repetitions for each inclusion position. Inclusion's depth is referred to the center of the black cylinder

the 'y' axis the mean value retrieved by the compact device and on the 'x' axis the one retrieved from the state-of-the-art system (nominal). Vertical error bars are relative to measurements performed with our compact system, while the radii of the semi-transparent disks represent the error bars of measurements performed using the state-of-art system. The semitransparent disks are centered both on y- and x-axis on the nominal phantom values retrieved by the state-of-the-art system. These results have to be compared with the values obtained by our compact TD-NIRS system (filled dots) in terms of linearity (closeness to the trend of the identity line), accuracy (position deviation from the center of semitransparent disks) and precision (dimension of the error bars). The error bars on the graphs can give us information on the coupling between μ_a and μ_s', the smaller the bars (or the disk) the better the uncoupling, taking into account that the measurements have been acquired with 1 s integration time and 20 repetitions for each phantom and both systems. Linearity can be assessed by retrieving the slope of the regression line (black dashed line) of the plotted data.

All data have been taken into account to determine the μ_s' regression line, while in the absorption plots, the values corresponding to the three highest μ_a values were excluded since we know that photon diffusion is less accurate for higher value of μ_a. The average accuracy (top-left corner in the graphs) is calculated as the relative error on the retrieved value with respect to the conventionally true one, overall, the 32 phantoms. Average accuracy is about 5% at 670 nm for both μ_a and μ_s', and 7% and 9% for μ_a and μ_s' at 830 nm, respectively.

4.4. Noise

The noise assay concerns the variability due to random effects that can occur by repeating a series of measurements on the same phantom. Noise behavior was studied as a function of the intensity of the detected optical signal, in terms of integrated counts in each DTOF [16]. Noise can be quantified defining the so-called "coefficient of variation" (CV), over the 20 repetitions, as:

$$CV = \frac{\sigma(x)}{\langle x \rangle}, \tag{3}$$

where x is the measurand (e.g., μ_a or μ_s'), σ denotes the standard deviation of x in the 20 repetitions and $\langle x \rangle$ denotes the corresponding average value. Figure 5 shows that the CV reaches acceptable values ($< 1\%$), for both μ_a and μ_s', when more than 450,000 photons are collected in
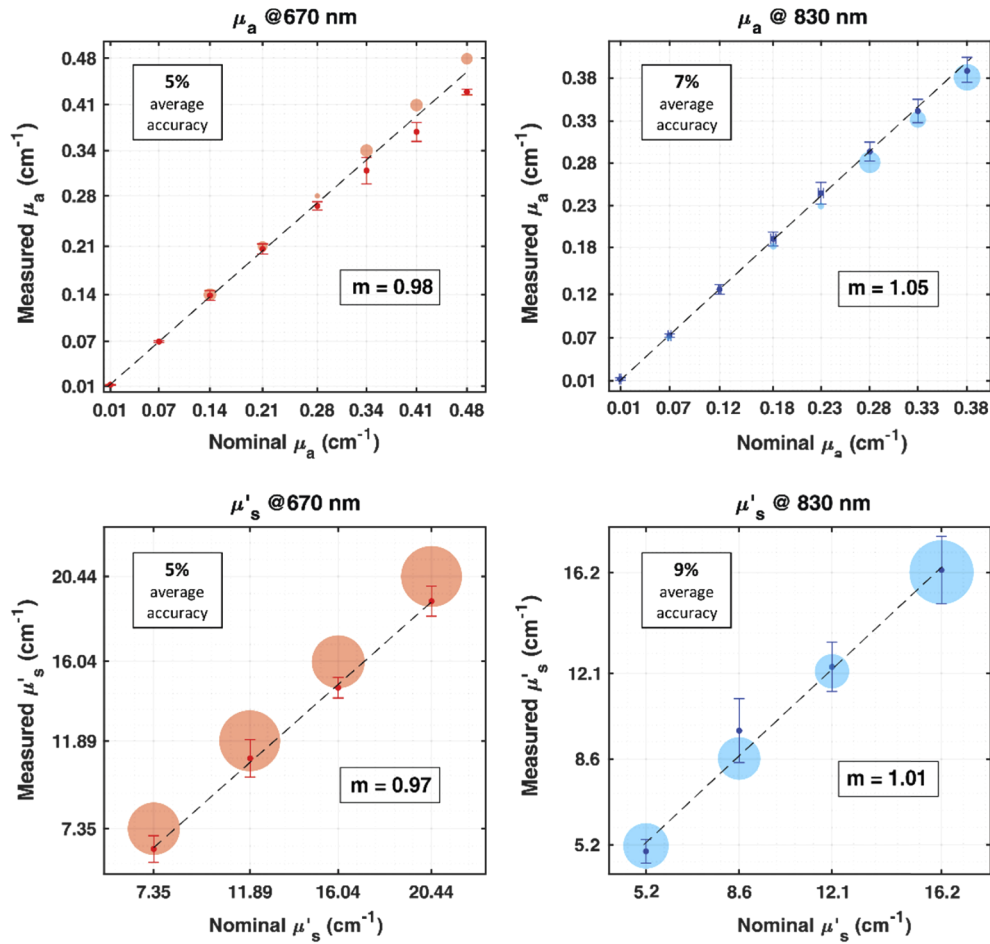
Fig. 4. Summary report of the MEDPHOT linearity for all 32 phantoms. Linearity plots of the measured μ_a (top) and μ_s' (bottom) for 670 nm (red) and 830 nm (blue). Conventionally true values are on the 'x' axis, and measured values (retrieved from our compact wearable system) are on the 'y' axis. The slope (m) of the regression line (dashed black line) indicates the overall linearity. Vertical error bars are relative to the compact system while, the radius of the semi-transparent disk is equal to the state-of-the-art system's error bars (on x-axis).

each DTOF. Low CV values will make the retrieval of the optical coefficients even more precise. Fitting of experimental points are in good accordance with the expected power law $x^{-0.5}$ which is the Poisson noise behavior. These results are in agreement with state-of-the-art systems based on the same acquisition technology.
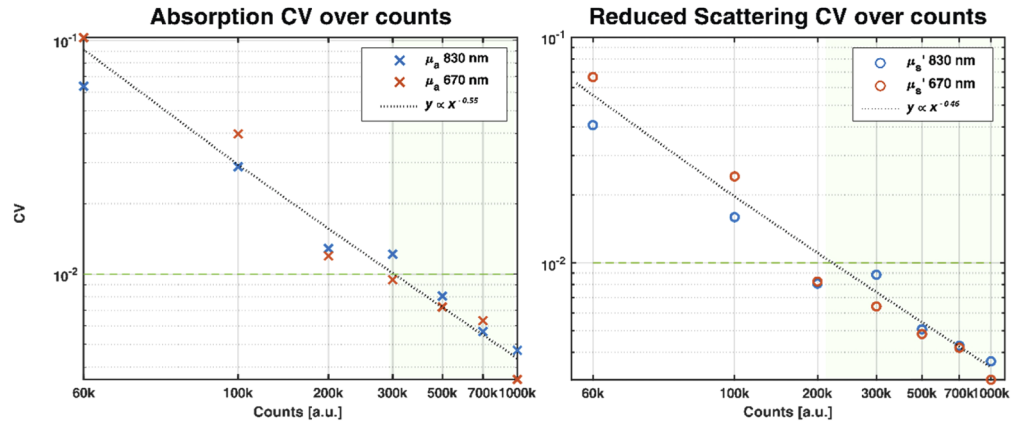
Fig. 5. CV over number of counts of the integrated DTOF for absorption (left side) ad reduced scattering coefficients (right side) at both wavelengths. The regions with CV values lower than 1% (dashed horizontal green line) are commonly considered as acceptable and are here highlighted with green shaded area. Data have been acquired with 20 repetitions for each wavelength with 1s integration time and 3 cm inter fiber distance. Black dotted lines represent the regression function retrieved from plotted data at both wavelengths.

4.5. Reproducibility and probe repositioning

The reproducibility analysis aims to assess the accordance between measurement results obtained, in identical experimental conditions, throughout different days (MEDPHOT Protocol [25]). The assay consisted of a measurement lasting 30 s with 500 ms acquisition per wavelength, each working day during a one-month period on the same tissue-mimicking phantom, ($\mu_a = 0.07$ cm^{-1}, $\mu_s' = 10$ cm^{-1}, nominal values at 660 nm). A conservative warm-up time of a least 15 minutes was ensured (see Section 4.1 for details on the system's warm-up time), and the probe was detached and replaced prior to each measurement. The results of the reproducibility analysis are reported in Table 1.

The CV for the absorption coefficient is lower than 1.5% for both wavelengths, whereas a maximum CV of 3% has been retrieved for the estimation of reduced scattering coefficient. To assess the variability of measurement results compared to the repositioning of the probe on the sample, a protocol, already used in similar studies [26] has been followed. The protocol consisted in 10 consecutive measurements, with 10 s measuring time each, in constant experimental condition, over a total period of 5 minutes. Between each measurement, the probe was taken off from the sample and placed back in the same position (within a time interval no longer than 20 s). The same phantom used in the reproducibility measurement was selected for this protocol. As reported in Table 1, the standard deviations and the CV related to the probe repositioning protocol are much lower than the ones obtained in the reproducibility measurements, being around 1%, in line with state-of-the-art TD-NIRS instruments [27].

4.6. Comparison between two replicas of the compact TD-NIRS device

A second replica of the compact TD-NIRS device has been fabricated to perform multi-channel *in-vivo* measurements. The components of both devices (A and B) were built and assembled

Table 1. Reproducibility and probe repositioning on phantoms[a]

	Measurand	Mean	Min – Max	Std	C.V. (%)
Reproducibility	μ_a (670) [cm^{-1}]	0.102	0.101 - 0.105	0.0013	1.3
	μ_a (830) [cm^{-1}]	0.094	0.093 - 0.095	0.0008	0.8
	μ_s' (670) [cm^{-1}]	11.0	10.8 - 11.4	0.20	1.8
	μ_s' (830) [cm^{-1}]	9.3	8.7 - 9.8	0.28	3.0
Probe repositioning	μ_a (670) [cm^{-1}]	0.103	0.101 - 0.106	0.0009	0.9
	μ_a (830) [cm^{-1}]	0.095	0.094 - 0.096	0.0006	0.6
	μ_s' (670) [cm^{-1}]	10.7	10.6 - 10.9	0.0007	0.7
	μ_s' (830) [cm^{-1}]	9.1	8.8 - 9.4	0.13	1.2

[a]**Reproducibility** measurements were performed on a tissue-mimicking phantom ($\mu_a = 0.07$ cm^{-1}, μ_s' $= 10$ cm^{-1}, nominal values at 660 nm). One measurement lasting 30 s was taken each day over a one-month period (0.5 s acquisition time and 10^6 counts per second per wavelength, 3 cm inter-fiber distance). **Probe repositioning** effects were measured on the same phantom. Ten 10-s measurements were taken every 20 seconds (0.5 s acquisition time and 10^6 counts per second per wavelength, 3 cm inter-fiber distance). The probe was detached from the sample and repositioned in between each measurement. The protocol duration was about 5 minutes long.

following the same procedures. A BIP characterization has been executed following the protocol depicted in [28], to verify the similarity in the performance of the two systems. The accordance between characteristics of the source and detector components, together with the temporal IRF can give us a first level assurance that the two systems will be able to retrieve consistent results. A responsivity measurement was performed on a dedicated phantom [28] and the two devices showed similar performance: system A, 2.19×10^{-8} m^{2}sr at 670 nm and 5.47×10^{-8} m^{2}sr at 830 nm; system B, 1.82×10^{-8} m^{2}sr at 670 nm and 5.44×10^{-8} m^{2}sr at 830 nm. This result was expected considering that same photodetection technology and same fibers types were used for both devices. In Fig. 6(a), the IRFs of system A and B for both wavelengths are reported. Each curve is the average of twenty acquisitions at 1 s integration time, with equal count rates. In Fig. 6(b), it is possible to appreciate the count distributions for uncorrelated illumination, resulting from the photon arrival-time measurement electronics of system A and B. The same integrated
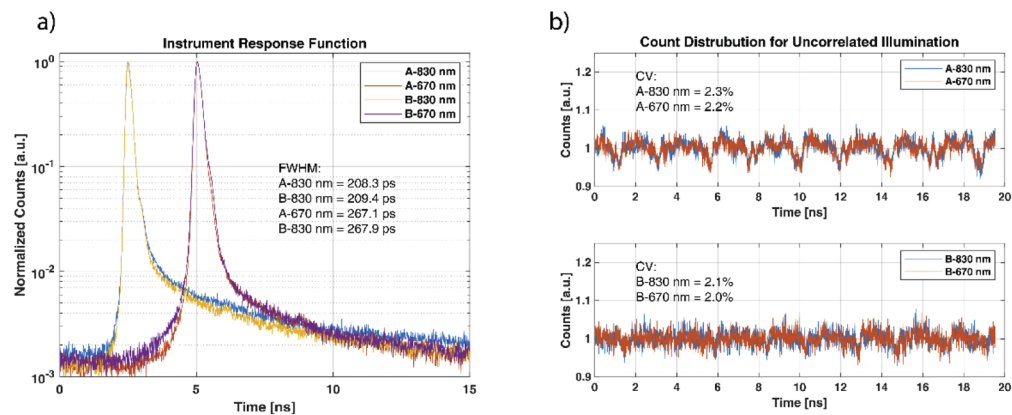
Fig. 6. Comparison between basic instrument performances. (a) Logarithmic plot of the instrument response function of system A and B for both wavelengths, the full width at half maximum of the IRFs are listed in the textbox. (b) Count distribution for uncorrelated illumination. Curves have been normalized over their mean values and plotted separately for the two systems. Textboxes show CVs for each system and each wavelength.

counts have been retrieved from the measurements, 1 s integration time for each wavelength in a 3 minutes long measure (180 repetitions). The curves are normalized over the mean values. The CV of the count distributions for uncorrelated illumination resulted comparable between the two devices and the different wavelengths. System A: 2.3% @ 830 nm, 2.2% @ 670 nm, and system B: 2.1% @ 830 nm, 2.0% @ 670 nm. Results of the basic instrument performance assessment suggest that the two systems have very similar features, we therefore expect to have comparable results in case of combined measurements. In this work, system B has been used, synchronous to system A, in the breath holding *in-vivo* exercise, presented in Section 5.3. All other data refer to system A.

5.   *In-vivo* experiments

The following paragraphs report a set of *in-vivo* experiments, performed with our portable TD-NIRS instruments. All subjects included in these measurements cooperated voluntarily and previously provided written informed consent to the procedures of the study, which was approved by the Ethics Committee of Politecnico di Milano.

5.1.   *Reproducibility and probe repositioning*

The *in-vivo* reproducibility was assessed by positioning the same probe used in phantom experiments on the forearm of a healthy volunteer (male, 25 years old). The subject was measured every day on the right arm, in the same location (marked on the skin with a long-lasting, skin-compatible, marking pen). The volunteer was asked to stay seated in resting position with the forearm leaning on a table for at least one minute before the measurement. To avoid hemodynamic changes induced by blood pressure variations, the height of the arm was set at the same height of the heart. In Table 2 (upper part), together with μ_s' and μ_a, we reported also the estimated values of O_2Hb, HHb, tHb, and StO_2, with mean values, min-max intervals, standard deviations, and CVs. It is worth noticing that CVs from reproducibility *in-vivo* are higher than CVs on phantoms. This is related to the intrinsic physiological variability of the subject over one-month period. In Table 2 (lower part), it is possible to appreciate the results related to the *in-vivo* probe repositioning experiment. In this assay, lasting approximately five minutes, ten measurements of 10 s were taken every 20 s (0.5 s acquisition time at 10^6 counts per second per wavelength, 3 cm inter-fiber distance). The probe was detached from the forearm and repositioned between different measurements. The variability during probe repositioning in hemodynamic parameters is well below 5%, which is identified in literature as the threshold for the clinical usability [29].

5.2.   *Finger tapping experiment*

For the finger tapping exercise, 3 different healthy volunteers (male, adults, 28, 48 and 50 years old) were measured. The experiment consisted of touching repetitively the tip of the thumb with the other fingers of the same hand, at a frequency of around 3 Hz, following a specific pattern: index, ring, middle, and pinky. The first part of the experiment the protocol consisted in 20 s of BASELINE (no movement) 20 s of TASK (performing the exercise) and 20 s of REST (recovery period), repeated 5 times, for a total of 5 minutes performed with the dominant hand. The start and stop signals were given vocally to the subjects, who were seated on a chair. In the second part, the same protocol has been followed with the other hand (non-dominant), while in a third part, still with a duration of 5 minutes, subjects were requested to stay still. The custom-made probe with 3 cm inter-fiber distance, has been placed over the motor cortex, upper limb area, on the opposite hemisphere compared to the dominant hand (contralateral) following the map of the 10/20 EEG system (e.g., C3 positioning for right-handed subjects). Therefore, task-related activations are expected during the first protocol part (contralateral probe positioning), while non-relevant activations are expected for the second (ipsilateral probe positioning) and third

**Table 2. Reproducibility and probe repositioning for in-vivo measurements**[b]

	Measurand	*Mean*	*Min – Max*	*Std*	*C.V. (%)*
Reproducibility	μ_a (670) [cm^{-1}]	0.64	0.54–0.71	0.045	7.0
	μ_a (830) [cm^{-1}]	0.42	0.39–0.46	0.017	4.0
	μ_s' (670) [cm^{-1}]	12.3	10.5–14.1	0.96	7.8
	μ_s' (830) [cm^{-1}]	7.1	6.1–7.9	0.48	6.8
	O_2Hb [µM]	124.5	109.5 - 146.3	10.4	8.3
	HHb [µM]	86.5	69.0 - 99.2	7.7	8.9
	tHb [µM]	211.0	198.6 - 230.7	7.2	3.4
	StO_2 (%)	58.9	52.5 - 68.0	3.9	6.6
Probe repositioning	μ_a (670) [cm^{-1}]	0.63	0.60–0.65	0.017	2.7
	μ_a (830) [cm^{-1}]	0.42	0.41–0.43	0.0061	1.4
	μ_s' (670) [cm^{-1}]	11.3	10.9–11.7	0.27	2.4
	μ_s' (830) [cm^{-1}]	6.5	6.4–6.7	0.096	1.5
	O_2Hb [µM]	128.2	123.1 - 132.8	3.5	2.7
	HHb [µM]	83.6	79.8 - 88.3	2.8	3.3
	tHb [µM]	211.9	206.2 - 216.1	2.8	1.3
	StO_2 (%)	60.5	58.2 - 62.5	1.3	2.2

[b]**Reproducibility** measurement was performed on a volunteer's forearm muscle. One measure lasting 30 seconds was taken each day over a one-month period (0.5 s acquisition time and 10^6 counts per second per wavelength, 3 cm inter-fiber distance). **Probe repositioning** effects were measured on a volunteer's forearm muscle. Ten measurements lasting 10 s were taken every 20 s (0.5 s acquisition time and 10^6 counts per second per wavelength, 3 cm inter-fiber distance). The probe was detached from the forearm and repositioned between different measurements. The protocol duration was about 5 minutes long.

(no movement) parts. The total measurement time was 15 minutes for each subject, while the integration time was set to 0.5 s for each wavelength. Activations of the upper limb motor cortex, related to finger tapping exercise, are expected to show an increase of the O_2Hb concentration and a decrease of the HHb concentration in the brain tissue during the task period. When the motor exercise ends, O_2Hb and HHb concentration values will tend to go back to the baseline [10,15,30]. Data have been plotted as variation from the baseline values and the results are shown in Fig. 7. It is possible to appreciate clear task-related activations in the contralateral configuration for each of the five tasks in all the three subjects, with a substantial contrast for both O_2Hb and HHb. Control measurements, in which the subjects were asked to not move (despite start and stop signals), show no task-related activation. Small ipsilateral activation can be seen on subject two, probably related to minor task-related systemic activity.

5.3. Breath holding experiment

In the breath holding experiment, three healthy volunteers (males, adults 25, 28 and 32 years old) were seated with the right arm laying on a table next to the chair at the same height of the heart. Two TD-NIRS wearable systems, with almost identical performance (see Section 4.6), were used to simultaneously monitor forearm muscle saturation and cerebral hemodynamics. The probe from the first instrument (A), used for brain monitoring, was placed on the prefrontal region Fp2 position of the 10/20 EEG system with 3 cm inter-fiber distance, while an identical probe, connected to the second instrument (B), was placed on the forearm muscle of the right arm, approximately 4 cm apart from the elbow junction, with the injection-detection axis perpendicular to the arterial cuff direction. In addition to the two TD-NIRS devices, a clinical-grade pulse-oximeter (VS-900, Mindray, Shenzhen, China) was used to monitor the
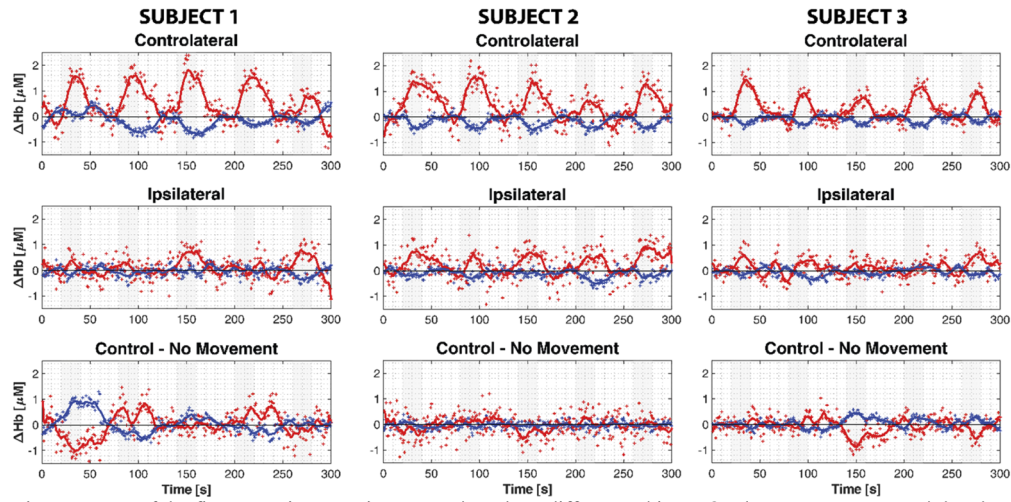
Fig. 7. Report of the finger tapping exercise protocol on three different subjects. On the rows are presented the plots for the contralateral and ipsilateral probe positions. Red crosses show the time behavior for O_2Hb while blue ones are relative to HHb. Straight lines over the crosses are results of a 7 s moving average. Time-resolved gated analysis has been used on raw data to retrieve hemoglobin variations in deep layers, reaching the motor cortex. The experiment protocol is 20s baseline, 20s task (gray area) and 20s recovery, repeated 5 times.

peripheral blood saturation on the first finger of the right arm. This set of measurements aimed to synchronously monitor different hemodynamic behaviors of muscles and brain tissues, during two subsequent tasks: one minute of deep breaths followed by a breath holding period. The protocol consisted of 60 s of BASELINE, 60 s of deep breaths, at a frequency of approximately 1/8 Hz (TASK1) and breath holding as long as subjects could (TASK2). The total measurement duration was 6 minutes, varying the final resting period to accommodate for the duration of TASK2, which was subject-dependent, ranging from 70 to 140 s. SpO_2 data coming from the pulse-oximeter were sampled every second. Results retrieved from the three subjects are reported in Fig. 8, showing the absolute values of the oxygen saturation in the three positions, finger (SpO_2), arm (StO_2) and head (StO_2). As expected, peripheral saturation shows higher values (normally ranging from 95% to 100% on healthy subjects) compared to tissue saturation. Results show that the arm tissue saturation follows the peripheral saturation behavior during TASK1, TASK2 and recovery period. In the case of brain tissue saturation, task-related hemodynamic variations seem to be opposite, though less substantial. Brain saturation seems to decrease during deep breathing and increase during breath holding. Our results are in line with previous studies in which peripheral and brain hemodynamic behaviors have been studied during breath holding task [31]. It is possible to hypothesize that brain tissue hemodynamics behaves differently, tending to preserve oxygenation at the expense of less critical or peripheral organs. However, given the very restricted cohort under study, no significant conclusions can yet be drawn.

5.4. Outdoor bike riding experiment

Our TD-NIRS wearable system was designed to be compact, lightweight, and rugged; it has therefore been tested in "out of the lab conditions", on freely moving subjects during an outdoor bike riding exercise. The experiment has been performed in a sunny summer day, 32 °C (90 °F) and the system was worn by the subjects as a small backpack (see Fig. 1(c)) while cycling. The system was battery operated and wirelessly controlled through a Wi-Fi connection from a laptop. A good connection was possible up to 40 m distance (in case of lost connection, the system was
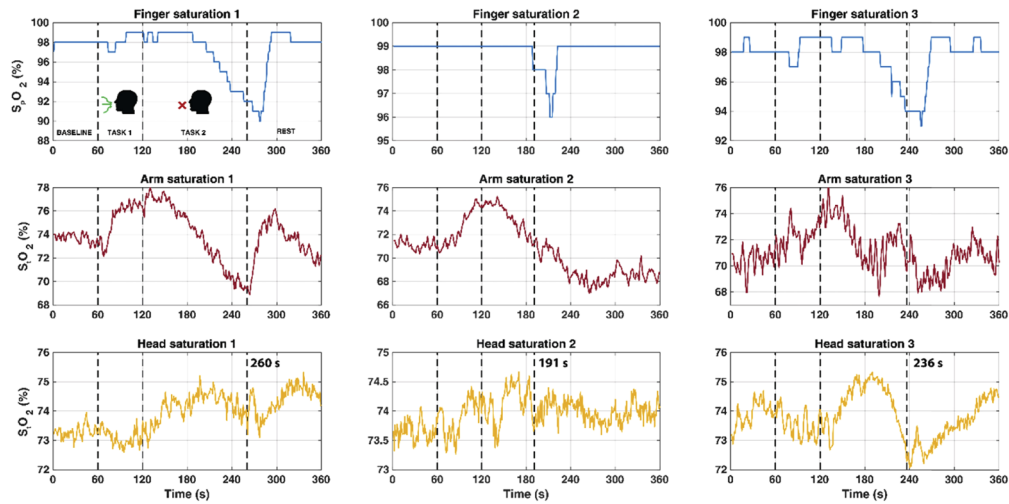
Fig. 8. Each column of the grid plot is referred to one volunteer and shows saturation behavior of the three investigated regions. Vertical dashed lines indicate boundaries between different periods of the measurement: baseline, deep breathing (TASK1), breath holding (TASK2) and recovery. The top row shows the peripheral saturation behavior (blue curve) measured on the index finger by the clinical-grade pulse-oximeter. The middle row presents the tissue saturation behavior of the forearm muscle (red curve, measured by system B), while the last row shows the brain tissue saturation behavior (yellow curve, measured by system A).

able to continue the data acquisition until the connection was restored). The probe position was on the vastus lateralis muscle of the dominant leg. Due to the high intensity of sunlight during the experiment, a black tissue was placed over the probe.

The protocol consisted of 60 s of BASELINE, with the subject standing still on both legs, followed by a 60 s of TASK, pedaling at approximately 0.5 Hz (riding at an average speed of 15 km/h) and a recovery period of 120 s, again standing on both legs. Task and recovery were repeated 5 times, with exception of the final recovery that lasted only 60 s. The experiment has been repeated on three healthy subjects (males, adults 25, 32 and 45 years old) with different overall physical training levels. Data were analyzed following the homogeneous media approximation. Results from the three subjects are shown in Fig. 9, where the concentration changes of O_2Hb and HHb are relative to the first averaged baseline values. Task-related variations are clearly visible in all repetitions, while consistent variations at the beginning and at the end of the task can also be noticed, especially on the O_2Hb. This is probably due to changes in the optical properties of the contracted muscle, compared to the relaxed state, together with higher proximity between probe and muscle tissue, due to the squeezing of the upper skin layer. It is interesting to see the behavior during the recovery period, different between the subjects, but reproducible over the repetitions. An overall trend is present in all the subjects, and it could be a symptom of the fatigue of the muscle, that is different for subjects with different physical performances. Finally, to verify system insensitivity to movement artifacts, the same protocol has been executed placing a tissue-mimicking phantom with a thickness of 1.5 cm ($\mu_a = 0.1$ cm^{-1}, $\mu_s' = 10$ cm^{-1}) between the probe and the vastus lateralis muscle. The thickness and the optical properties of the phantom are sufficient to avoid that a significant number of photons probe the muscle. Given that the phantom keeps constant optical properties during the bike riding exercise, all deviations from the baseline values must be attributed to artifacts due to movements of probe, fibers and in general the whole system hold on the subject's shoulders. Optical coefficients retrieved from the

measurements were translated into O_2Hb and HHb concentration variations and reported in the graph entitled "CONTROL" in Fig. 9. The calculation of pseudo O_2Hb and HHb changes for the phantom has been performed to compare this plot more easily with the subject's ones. From the graph, it is possible to appreciate that there is no substantial variation of O_2Hb and HHb from baseline values, suggesting that our measurements do not present motion artifacts related to leg movements during pedaling.
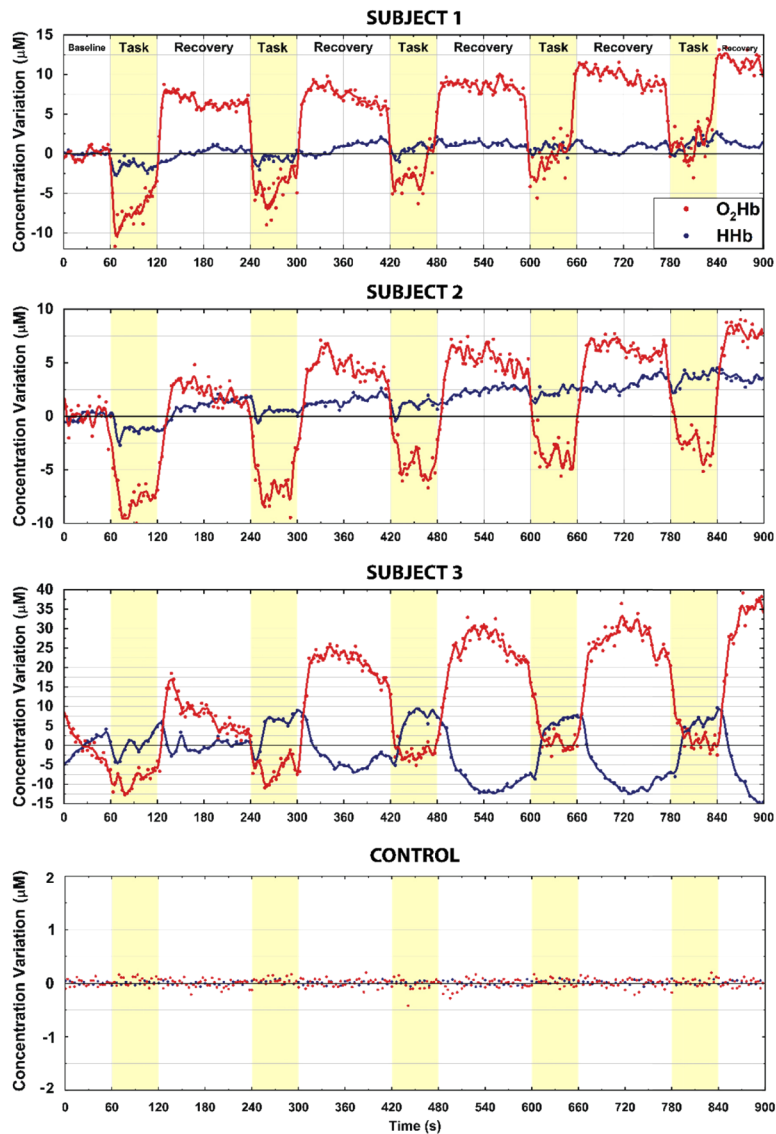
Fig. 9. Report of the outdoor bike riding protocol, the first three plots are related to the three subjects. After 60 s baseline, the Task-Recovery period is repeated 5 times. Task sections are highlighted in yellow color. The blue curve (deoxy-hemoglobin concentration) and red curve (oxy hemoglobin concentration) are retrieved from the data points by moving average algorithm on 3 neighbors spots. The last plot shows the results of the control measurement. The same protocol was performed on subj number three with a tissue mimicking phantom placed between the probe and the muscle.

6.   Conclusions

We presented an innovative TD-NIRS wearable system, fully validated and characterized following consolidated protocols and tested in *in-vivo* experiments on freely moving subjects, both on brain ad muscle tissues. The instrument shows excellent results in terms of stability, depth sensitivity, linearity, accuracy, and reproducibility. Preliminary *in-vivo* experiments, exploiting also two identical synchronized devices, showed the possibility to effectively retrieve tissue hemodynamics in either monitoring applications or functional task-related protocols. Thanks to customized probes and a tailored backpack mount, it was also possible to follow muscle hemodynamics during outdoor activity, such as bike riding. The system proves to be accurate, sensitive to real-time deep hemodynamic variations, and rugged. These features are very interesting in many different applications such as neuro-functional monitoring and sport. Its compactness, lightweight, and easy probe positioning make the device suitable to be used also by non-expert of the diffuse-optics field.

Funding

Acknowledgments

Disclosures

M.L., M.B., A.D.M., F.Z., A.P, A.T., A.T. and D.C.: pioNIRS, Italy (I). Other authors declare that there are no conflicts of interest related to this article.

References

1. T. Durduran, R. Choe, W. B. Baker, and A. G. Yodh, "Diffuse optics for tissue monitoring and tomography," Rep. Prog. Phys. **73**(7), 076701 (2010).
2. F. Jobsis, "Noninvasive, infrared monitoring of cerebral and myocardial oxygen sufficiency and circulatory parameters," Science **198**(4323), 1264–1267 (1977).
3. M. Ferrari, "Progress of near-infrared spectroscopy and topography for brain and muscle clinical applications," J. Biomed. Opt. **12**(6), 062104 (2007).
4. F. Scholkmann, S. Kleiser, A. J. Metz, R. Zimmermann, J. Mata Pavia, U. Wolf, and M. Wolf, "A review on continuous wave functional near-infrared spectroscopy and imaging instrumentation and methodology," Neuroimage (2014).
5. A. Torricelli, D. Contini, A. Pifferi, M. Caffini, R. Re, L. Zucchelli, and L. Spinelli, "Time domain functional NIRS imaging for human brain mapping," NeuroImage **85**, 28–50 (2014).
6. F. Martelli, T. Binzoni, A. Pifferi, L. Spinelli, A. Farina, and A. Torricelli, "There's plenty of light at the bottom: Statistics of photon penetration depth in random media," Sci. Rep. (2016).
7. D. Contini, L. Spinelli, A. Torricelli, A. Pifferi, and R. Cubeddu, "Novel method for depth-resolved brain functional imaging by time-domain NIRS - art. no. 662908," Diffus. Opt. Imaging Tissue (2007).
8. M. Buttafava, E. Martinenghi, D. Tamborini, D. Contini, A. D. Mora, M. Renna, A. Torricelli, A. Pifferi, F. Zappa, and A. Tosi, "A Compact Two-Wavelength Time-Domain NIRS System Based on SiPM and Pulsed Diode Lasers," IEEE Photonics J. **9**(1), 1–14 (2017).
9. M. Lacerenza, M. Buttafava, M. Renna, L. Marchesi, A. Torricelli, and A. Tosi, "Wearable time domain near infrared spectroscopy system," **11237**, 112(July), (2020).
10. D. Contini, A. Torricelli, A. Pifferi, L. Spinelli, F. Paglia, and R. Cubeddu, "Multi-channel time-resolved system for functional near infrared spectroscopy," Opt. Express (2006).
11. E. Martinenghi, A. Dalla Mora, D. Contini, A. Farina, F. Villa, A. Torricelli, and A. Pifferi, "Spectrally Resolved Single-Photon Timing of Silicon Photomultipliers for Time-Domain Diffuse Spectroscopy," IEEE Photonics J. (2015).
12. E. Martinenghi, L. Di Sieno, D. Contini, M. Sanzaro, A. Pifferi, and A. Dalla Mora, "Time-resolved single-photon detection module based on silicon photomultiplier: A novel building block for time-correlated measurement systems," Rev. Sci. Instrum. (2016).

13. B. Markovic, S. Tisa, F. A. Villa, A. Tosi, and F. Zappa, "A high-linearity, 17 ps precision time-to-digital converter based on a single-stage vernier delay loop fine interpolation," IEEE Trans. Circuits Syst. I Regul. Pap. (2013).
14. R. Cubeddu, A. Pifferi, P. Taroni, A. Torricelli, and G. Valentini, "Experimental test of theoretical models for time-resolved reflectance," Med. Phys. **23**(9), 1625–1633 (1996).
15. L. Zucchelli, D. Contini, R. Re, A. Torricelli, and L. Spinelli, "Method for the discrimination of superficial and deep absorption variations by time domain fNIRS," Biomed. Opt. Express **4**(12), 2893 (2013).
16. A. Pifferi, A. Torricelli, A. Bassi, P. Taroni, R. Cubeddu, H. Wabnitz, D. Grosenick, M. Möller, R. Macdonald, J. Swartling, T. Svensson, S. Andersson-Engels, R. L. P. van Veen, H. J. C. M. Sterenborg, J.-M. Tualle, H. L. Nghiem, S. Avrillier, M. Whelan, and H. Stamm, "Performance assessment of photon migration instruments: the MEDPHOT protocol," Appl. Opt. **44**(11), 2104 (2005).
17. H. Wabnitz, D. R. Taubert, M. Mazurenka, O. Steinkellner, A. Jelzow, R. Macdonald, D. Milej, P. Sawosz, M. Kacprzak, A. Liebert, R. Cooper, J. Hebden, A. Pifferi, A. Farina, I. Bargigia, D. Contini, M. Caffini, L. Zucchelli, L. Spinelli, R. Cubeddu, and A. Torricelli, "Performance assessment of time-domain optical brain imagers, part 1: basic instrumental performance protocol," J. Biomed. Opt. **19**(8), 086010 (2014).
18. H. Wabnitz, A. Jelzow, M. Mazurenka, O. Steinkellner, R. Macdonald, D. Milej, N. Zolek, M. Kacprzak, P. Sawosz, R. Maniewski, A. Liebert, S. Magazov, J. Hebden, F. Martelli, P. Di Ninni, G. Zaccanti, A. Torricelli, D. Contini, R. Re, L. Zucchelli, L. Spinelli, R. Cubeddu, and A. Pifferi, "Performance assessment of time-domain optical brain imagers, part 2: nEUROPt protocol," J. Biomed. Opt. **19**(8), 086012 (2014).
19. I. Pirovano, R. Re, A. Candeo, D. Contini, A. Torricelli, and L. Spinelli, "Instrument response function acquisition in reflectance geometry for time-resolved diffuse optical measurements," Biomed. Opt. Express **11**(1), 240 (2020).
20. F. Martelli, A. Pifferi, D. Contini, L. Spinelli, A. Torricelli, H. Wabnitz, R. Macdonald, A. Sassaroli, and G. Zaccanti, "Phantoms for diffuse optical imaging based on totally absorbing objects, part 1: basic concepts," J. Biomed. Opt. **18**(6), 066014 (2013).
21. S. Konugolu Venkata Sekar, A. Dalla Mora, I. Bargigia, E. Martinenghi, C. Lindner, P. Farzam, M. Pagliazzi, T. Durduran, P. Taroni, A. Pifferi, and A. Farina, "Broadband (600-1350 nm) Time-Resolved Diffuse Optical Spectrometer for Clinical Use," IEEE J. Sel. Top. Quantum Electron. **22**(3), 406–414 (2016).
22. M. Alayed, D. P. Palubiak, and M. J. Deen, "Characterization of a Time-Resolved Diffuse Optical Spectroscopy Prototype Using Low-Cost, Compact Single Photon Avalanche Detectors for Tissue Optics Applications," Sensors (Basel). (2018).
23. L. Di Sieno, N. G. Boetti, A. Dalla Mora, D. Pugliese, A. Farina, S. Konugolu Venkata Sekar, E. Ceci-Ginistrelli, D. Janner, A. Pifferi, and D. Milanese, "Towards the use of bioresorbable fibers in time-domain diffuse optics," J. Biophotonics (2018).
24. A. Pifferi, A. Torricelli, P. Taroni, D. Comelli, A. Bassi, and R. Cubeddu, "Fully automated time domain spectrometer for the absorption and scattering characterization of diffusive media," Rev. Sci. Instrum. (2007).
25. A. Pifferi, A. Torricelli, A. Bassi, P. Taroni, R. Cubeddu, H. Wabnitz, D. Grosenick, M. Möller, R. Macdonald, J. Swartling, T. Svensson, S. Andersson-engels, R. L. P. Van Veen, H. J. C. M. Sterenborg, J. Tualle, H. L. Nghiem, S. Avrillier, M. Whelan, and H. Stamm, "Performance assessment of photon migration instruments: the MEDPHOT protocol," (2005).
26. B. Andresen, A. De Carli, M. Fumagalli, M. Giovannella, T. Durduran, U. Michael Weigel, D. Contini, L. Spinelli, A. Torricelli, and G. Greisen, "Cerebral oxygenation and blood flow in normal term infants at rest measured by a hybrid near-infrared device (BabyLux)," Pediatr. Res. (2019).
27. M. Giovannella, "The BabyLux device: a diffuse optical system integrating diffuse correlation spectroscopy (DCS) and time resolved near infrared spectroscopy (TRS) for neuro-monitoring of the premature newborn brain," (n.d.).
28. H. Wabnitz, D. R. Taubert, M. Mazurenka, O. Steinkellner, A. Jelzow, R. Macdonald, D. Milej, P. Sawosz, M. Kacprzak, A. Liebert, R. Cooper, J. Hebden, A. Pifferi, A. Farina, I. Bargigia, D. Contini, M. Caffini, L. Zucchelli, L. Spinelli, R. Cubeddu, and A. Torricelli, "Performance assessment of time-domain optical brain imagers, part 1: basic instrumental performance protocol," J. Biomed. Opt. **19**(8), 086010 (2014).
29. L. C. Sorensen and G. Greisen, "Precision of measurement of cerebral tissue oxygenation index using near-infrared spectroscopy in preterm neonates," J. Biomed. Opt. **11**(5), 054005 (2006).
30. M. Lacerenza, M. Buttafava, M. Renna, L. Marchesi, A. Torricelli, and A. Tosi, "A wearable time domain near-infrared spectroscopy system," 1107**404**(July), (2019).
31. J. Bouten, J. G. Bourgois, and J. Boone, "Hold your breath: peripheral and cerebral oxygenation during dry static apnea," Eur. J. Appl. Physiol. (2020).